

Particle–fluid velocities and fouling in rotating filtration of a suspension

Steven T. Wereley^a, Alp Akonur^b, Richard M. Lueptow^{c,*}

^a School of Mechanical Engineering, Purdue University, 1288 Mechanical Engineering Building, West Lafayette, IN 47907, USA

^b Baxter Healthcare Corp., Round Lake, IL 60073, USA

^c Department of Mechanical Engineering, Northwestern University, 2145 Sheridan Road, Evanston, IL 60208, USA

Received 23 January 2002; received in revised form 30 May 2002; accepted 10 June 2002

Abstract

The flow of dilute suspensions in a rotating filter separator consisting of a rigid, porous, polyethylene cylindrical filter rotating within an outer cylindrical shell was studied using laser-based velocity measurement techniques. The centrifugal instability of the Taylor–Couette flow results in toroidal vortices stacked in the annulus. The velocity field of the particles is very similar to that of the fluid indicating that the vortical structure readily entrains particles. Profiles of the concentration of particles in the device show that the particles tend toward a concentration polarization layer near the porous inner cylinder due to the radial flow, but the concentration in the layer is reduced as the velocity gradient near the wall is increased. This steep velocity gradient is a consequence of the vortices in the flow redistributing the azimuthal momentum. The vortices also distribute the particles uniformly across the annulus between the porous inner cylinder and the outer shell. Particles typically form a thin cake on the inner cylinder due to the radial flow. However, there is a critical Taylor number, which is related to the rotational speed of the inner cylinder, above which the particles are swept off of the inner cylinder and resuspended in the vortical flow.

© 2002 Elsevier Science B.V. All rights reserved.

Keywords: Microfiltration; Dynamic filtration

1. Introduction

Rotating filter separation is an innovative filtration technology that could provide cost-effective separation, concentration, and clarification in a wide range of applications, because it appears to be superior to other types of filtration in the slowing of plugging of the filter pores [1–8]. A cylindrical rotating filter separator consists of a porous cylinder rotating within a concentric non-porous cylinder. A suspension enters

the top of the annulus between the coaxial cylinders and travels axially in the annulus. The filtrate passes through the porous inner cylinder and is channeled to the hollow shaft supporting the inner cylinder where it exits at the bottom of the device. The suspension becomes increasingly concentrated as it moves along the annulus. Finally, the concentrated suspension exits at the bottom of the annulus. Because the fluid flow in a rotating filter separator minimizes the plugging of the pores of the filter, substantially less filter area is needed than with traditional cross-flow filtration to achieve the same throughput, at least for the present application of rotating filter separation of blood [6,9]. Furthermore, the filter medium of a rotating filter needs cleaning or

* Corresponding author. Tel.: +1-847-491-4265;

fax: +1-847-491-3915.

E-mail address: r-lueptow@northwestern.edu (R.M. Lueptow).

Nomenclature

d	annular gap width
D_p	particle diameter
F_τ	force due to shear
F_D	force due to Stokes drag
r	radial coordinate
r_i	radius of inner cylinder
r_o	radius of outer cylinder
Re_a	axial Reynolds number (Wd/ν)
Re_r	radial Reynolds number (Ud/ν)
St	Stokes number
Ta	Taylor number ($r_i\Omega d/\nu$)
Ta_{crit}	critical Taylor number for the appearance of vortices
U	radial velocity
v_f	fluid velocity
v_p	particle velocity
W	axial velocity
z	axial coordinate

Greek letters

Ω	angular velocity
η	radius ratio (r_i/r_o)
μ	dynamic viscosity
ν	kinematic viscosity
θ	tangential coordinate
ρ_p	particle density

replacement less frequently because the pores of the filter plug with particles more slowly than in standard cross-flow filtration.

A handful of studies have evaluated the performance of rotating filter separators for specific separation applications. Rotating filter separators were first tested for skim milk separation [1,10] and for fermentation [2]. The device has also been tested for use in oil–water separation [3,11] and concentration of biological suspensions [4,5,12–14]. Several studies have also addressed the performance of a commercial rotating filter separator for separating plasma from whole blood [15–17]. Key to these studies is interest in Taylor vortices, a stack of toroidal vortices that appear in the annulus between a rotating inner cylinder and a stationary outer cylinder above a critical speed as a result of a centrifugal instability, or on the effectiveness of using the device for particular applications.

Several engineering analyses and experiments on the blood plasma separation system using rotating filtration have been done. It has been shown that the filtrate flux rate using a commercial plasma separator based on rotating filtration is one to two orders of magnitude higher than that for traditional cross-flow filtration of blood [6,18]. Beaudoin and Jaffrin [9] provided some evidence that the action of Taylor vortices is more important than the centrifugal sedimentation of the particles on the anti-fouling nature of the device. In addition, mathematical models of the filtration flow have been proposed that use relatively simple models for the effect of the supercritical Taylor vortices [6,19]. Perhaps, the most thorough work on rotating filtration was done by the Belfort group, both modeling and experiments [20,21]. Their work, which was focused on the membrane–particle interaction, indicated that particle intrusion into pores of the rotating membrane was the dominant type of fouling.

Of course, the two-phase character of the suspension is key to the underlying physics of the flow and separation. The rotation of the porous inner cylinder results in a flow configuration that is similar to cross-flow filtration except that the filter moves past the suspension rather than the suspension flowing parallel to the filter surface. The higher concentration of particles near the filter surface and the deposition of particles on the surface, or cake layer, are reduced by the shear. At a microscopic level, a single particle travels generally parallel to the surface of the filter until it reaches the pore where some of the fluid is sucked into the pore. A particle that is carried with the fluid has several forces acting on it. Drag and lift forces result from the fluid motion. A body force results from the centrifugal field if the particle has a different density than the fluid. Thus, very near to where the fluid is sucked into a pore, the centrifugal body force along with shear induced lift forces and other back-transport mechanisms tend to drive a particle that is denser than the fluid away from the pore. The interplay between these forces depends on the particle and fluid densities, the particle and pore sizes, and the fluid flow field. Away from the pore, the lift and drag due to the Taylor vortex flow and the centrifugal forces affect the particle motion. The Taylor vortices were originally thought to wash particles off the filter [12], but have more recently been shown to simply redistribute azimuthal momentum thereby increasing the shear at

the porous inner cylinder [22–25]. Recent analytical results indicate that the interaction of forces on a particle results in particles tending toward a limit cycle orbit within a Taylor vortex that is not near the walls of the annulus [26]. Our recent experiments covering a wide range of rotational speeds, particles, fluids, and flow rates indicate that the key factor in preventing fouling is the high rotational shear enhanced by the redistribution of azimuthal momentum by the vortices and supplemented by the shear due to the axial flow and centrifugal sedimentation [25].

In this paper, we present measurements in which we independently track the fluid and the particle motion in a rotating cylindrical filter using two laser-based velocity measure techniques, particle image velocimetry (PIV) and particle tracking velocimetry (PTV). To track both fluid and particle motion we use two classes of particles: small PIV “tracer particles” to follow the fluid flow and larger “inertial particles” as the particulate phase of the suspension. In addition, the images obtained for PIV and PTV were interrogated to determine the particle concentration profiles in a rotating filter device. Our goal here is to determine how closely the particles in the flow follow the fluid and to examine the anti-fouling nature of cylindrical rotating filter devices.

2. Experimental apparatus and procedure

The flow system consisted of two concentric cylinders, an inner rotating rigid, porous, polyethylene cylinder and an outer glass cylinder with radii $r_i = 4.23$ cm and $r_o = 5.22$ cm, respectively as shown in Fig. 1. The resulting gap width was $d = r_o - r_i = 0.99$ cm, and the radius ratio was $\eta = r_i/r_o = 0.81$. The inner cylinder assembly consisted of a rigid, porous, polyethylene cylindrical sleeve with a wall thickness of 0.6 cm fitted over an aluminum cylinder, which was mounted on a hollow stainless steel shaft. The porous cylinder had a nominal pore size of $5 \mu\text{m}$, a porosity of 20–30%, a specific density of 0.94–0.95, and a permeability of $7.8 \times 10^{-9} \text{ cm}^2$. The inner cylinder was driven by a stepper motor capable of microstepping at 25 000 steps per revolution allowing computer control of the rotational speed of the inner cylinder to better than 0.1%. The two cylinders were held concentric by aluminum endcaps. The ratio

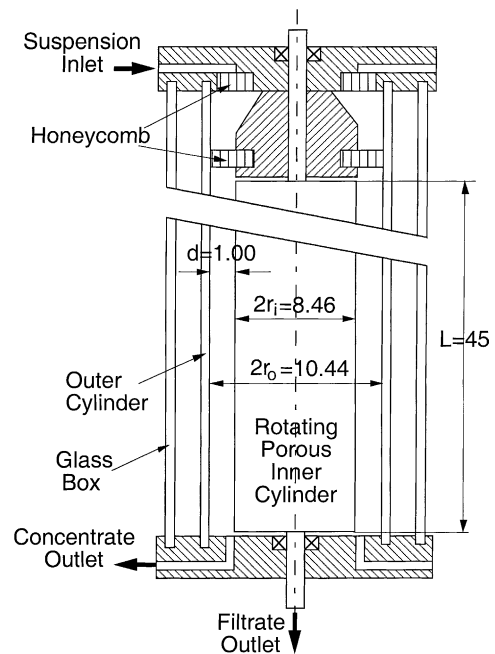


Fig. 1. Sketch of the experimental set-up. Dimensions are in centimeters.

of the length of the annulus to the gap width was 45–48, depending on details of the individual test. For some tests where the radial flow was set to zero, a non-porous inner cylinder with diameter $r_i = 4.34$ cm was used, resulting in a radius ratio of $\eta = 0.83$, an inconsequential difference with respect to the flow.

The working fluid flowed from an upper constant head reservoir into a deep annular groove in the upper endcap through four tangential inlet ports. This provided a transmembrane pressure of about 20 kPa. The fluid then passed through a flow-straightening section in the upper endcap consisting of two honeycomb sections (0.5 cm thick with a cell diameter of 0.1 cm) on either side of a 2:1 contraction section to straighten the flow and to provide an end boundary condition of nearly pure axial flow with minimal radial and azimuthal velocity components. The fluid exited the annulus via a deep annular groove in the lower endcap with four radially oriented outlets. Fluid could also pass radially through the porous sleeve of the inner cylinder and then axially along an annular channel between the porous sleeve and the aluminum cylinder, and finally radially inward through four holes

to a hollow shaft where it exited the flow cell. The volume flow rate was controlled by a valve below the flow cell and was measured with electromagnetic or turbine flowmeters at the two outlets of the flow cell. Fluid exited to a lower reservoir and was recirculated to the upper constant-head reservoir with a pump.

Two separate sets of experiments were performed, one measuring velocities in the meridional ($r-z$) plane and one measuring velocities in the latitudinal ($r-\theta$) plane. For a variety of practical reasons related to the experimental apparatus and techniques, different working fluids and particles were used in each case. For the meridional plane measurements, the working fluid was a mixture of water, glycerol, sodium iodide, and trace amounts of sodium thiosulfate to prevent a yellowish tint in the solution [27]. The sodium iodide was used to increase the index of refraction of the fluid to match that of glass (1.47), so that the laser beam was not refracted at the curved fluid–glass interface. The fluid had a density of 1620 kg/m^3 (1.62 g/cm^3) and nominal viscosity of $\nu = 3.15 \times 10^{-6} \text{ m}^2/\text{s}$ (3.15 cSt).

To track both fluid and particle motion we use two classes of particles: small PIV “tracer particles” to follow the fluid flow and larger “inertial particles” as the particulate phase of the suspension. We differentiate between the two types of particles in this way to suggest that tracer particles follow the fluid flow exactly by acting like fluid particles, which ideally have infinitesimal size and a density identical to the fluid. Inertial particles have a finite size and may have a density different from the fluid, so they may not follow the fluid flow exactly. Fluorescent polystyrene latex spheroids (provided by Professor Joseph Katz, Johns Hopkins University) with an average diameter of $25 \mu\text{m}$ and a density of 1100 kg/m^3 (1.1 g/cm^3) were added as PIV tracer particles. These particles absorb 520 nm light most efficiently and emit light at 630 nm. For the latitudinal plane measurements, the working fluid was a 40% glycerol water mixture [1090 kg/m^3 (1.09 g/cm^3) and $3.7 \times 10^{-6} \text{ m}^2/\text{s}$ (3.7 cSt)] with 10–14 μm hollow glass spheres [1100 kg/m^3 (1.1 g/cm^3)] as PIV tracer particles. In both cases, based on an analysis of how well particles follow a flow [28], the tracer particles are small enough to follow fluid velocity oscillations up to very high frequency in spite of the density differences with the fluid. Furthermore, the axial flow in the flow cell kept these particles in suspension.

For the meridional plane measurements, the larger inertial particles used as the particulate phase were approximately $300 \mu\text{m}$ diameter Saran particles with a density of 1630 kg/m^3 (1.63 g/cm^3). For the latitudinal plane measurements, the inertial particles were approximately $150 \mu\text{m}$ PMMA spherical particles with a density of 1200 kg/m^3 (1.2 g/cm^3). The fractional volume concentration of the larger particles was near 0.05 for the meridional plane experiments and 0.0001 for the latitudinal plane experiments to avoid speckle noise that degraded the PIV measurements. The speckle noise was most problematic for the latitudinal plane experiments, since light reflected from the particles in the laser sheet traveled through a significant distance in the suspension.

For a given experiment, adjusting the appropriate valves set the axial and radial flow rates. Then the speed of the inner cylinder was ramped linearly to the desired speed and the flow was allowed to develop for at least as long as the mean residence time of the suspension, which ranged from 1 to 10 min. In some cases, it was necessary to readjust the valves and allow the flow to develop after the inner cylinder reached the desired speed due to changes in pressure drop with flow state.

PIV and PTV depend on the illumination of a plane in the flow with a sheet of laser light. For the meridional ($r-z$) plane measurements, the outer cylinder was surrounded a glass box filled with a refractive index matched fluid to prevent refraction at the curved surface of the outer cylinder. An electronically shuttered 10 W argon laser was used to illuminate a radial–axial plane through the axis of the cylindrical Couette flow device. Since the through-sheet velocity in the azimuthal direction was so much larger than the measured axial and radial velocities, care was taken to assure that the laser sheet timing was short enough and the laser intensity great enough to capture a largely overlapping population of particles in two consecutive images. For the latitudinal plane measurement, a 25-mJ per pulse dual YAG pulsed laser system was used to illuminate a latitudinal ($r-\theta$) plane in the flow. In this case, the light reflected from the particles was imaged through a flat window in the endwall, making the glass box surrounding the experiment unnecessary.

A CCD camera (TSI Inc.) positioned perpendicular to the laser sheet was used to record the flow in the plane illuminated by the laser sheet. For the

meridional plane experiments, the region that was imaged was at a location about one-third of the total flow cell length from the exit of the device. For the latitudinal plane experiments, the laser sheet was positioned about one-quarter of the total flow cell length from the exit of the device. In both cases, the flow was fully developed at the measurement location. Approximately 150–160 image pairs were captured at a net rate of 15 Hz. For the meridional plane measurements, images of the small fluorescing tracer particles were obtained by using a filter that stopped blue–green argon-ion laser light but passed the red light emitted by the tracer particles. Fluid velocity vectors based on the tracer particles were calculated on a rectangular grid of points using standard PIV techniques. PIV is based on the cross-correlation of small regions of consecutive digital images of the tracer particles. The average displacement of the particles from the first image to the second image results in a peak in the two-dimensional cross-correlation from which the average velocity of the tracer particles, and hence the fluid, can be obtained. Images of the larger particles were obtained at reduced laser intensity with no optical filter. At this light level, the light reflected and emitted from the small fluorescing tracer particles was too dim to be recorded by the camera. Again PIV was used to find the velocity, this time of the larger particles. Thus, it was possible to record the velocity of the two classes of particles separately. For the latitudinal plane measurements, the CCD camera was positioned to view through a clear window in the lower endcap of the test cell. In this case, images of both particles were obtained simultaneously. The larger particles were identified based on the brightness and size of the particles in the image, and their locations were recorded. Then an image with the large particles removed leaving only PIV tracer particles was created for PIV analysis to obtain the fluid velocity. Using the locations of the larger particles and the PIV velocity field, the velocity of individual large inertial particles was obtained using particle tracking velocimetry (PTV) in which the positions of individual particles are tracked in consecutive images of the illuminated plane [29].

The flow is characterized by three dimensionless flow parameters. The ratio of centrifugal to viscous forces is represented by the Taylor number, $Ta = r_1 \Omega d / \nu$, where r_1 is the radius of the inner cylinder

and Ω is the rate of rotation of the inner cylinder. The axial Reynolds number is $Re_a = W(z)d/\nu$, where W is the radially averaged axial velocity as a function of axial measurement position z . The radial Reynolds number is $Re_r = Ud/\nu$, where U is the average radial velocity. (The inner porous cylinder provides a high resistance to the flow, and the pressure gradient along the length of the annulus is small. Taken together, these suggest a relatively uniform flux through the inner cylinder.) The Taylor number was varied from 0 to 1650, corresponding to cross-flow velocities of 0–0.5 m/s; the axial Reynolds number was varied from 0 to 80, corresponding to cross-flow velocities of 0 to 0.025 m/s; the radial Reynolds number was varied from 0 to 0.86, corresponding to radial velocities of 0 to 2.7×10^{-4} m/s. These conditions span a large parameter space that includes that for commercial rotating filters, such as those used for separating plasma from blood (Plasmacell, Baxter Healthcare Corporation). In this case, $100 < Ta < 500$, $1 < Re_a < 5$, and $0.003 < Re_r < 0.007$. Note that the axial Reynolds number can vary somewhat with position along the length of the annulus due to the removal of fluid by the radial flow.

The flow in the annulus is strongly dependent upon the flow parameters. Above the critical Taylor number, $Ta_{crit} = 97$ for the radius ratio in these experiments, toroidal Taylor vortices appear in the annulus. This

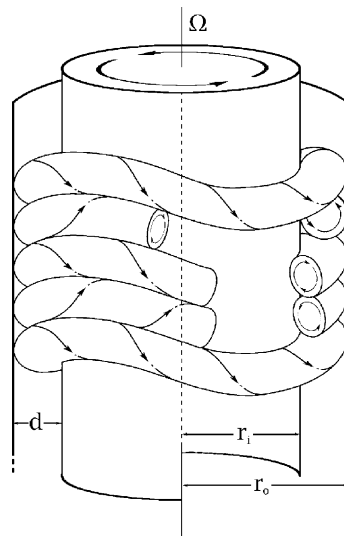


Fig. 2. A schematic representation of wavy vortex flow.

critical Taylor number is altered only slightly when a radial or axial flow is present [30]. At slightly higher Taylor numbers the vortices develop an azimuthal waviness with an axial distortion, as shown schematically in Fig. 2. These waves travel around the annulus in the same direction as the rotation of the inner cylinder with a velocity from about one-third to one-half that of the inner cylinder [31,32]. The axial velocity causes these wavy vortices to translate axially with approximately the speed of the axial flow [33,34].

3. Fluid and particle velocity fields

A typical flow pattern in a meridional plane for zero radial flow along with a low axial flow ($Re_a = 3$ at the axial measurement location) and a moderate Taylor number corresponding to wavy vortex flow ($Ta = 314$) is shown in Fig. 3(a). In this and subsequent figures, the velocity field at five time instants is shown with time progressing from top to bottom. Eight time instants correspond to the period of one

azimuthal wave of the wavy vortex. The axial flow is left to right, but the axially averaged mean axial velocity profile has been subtracted from the velocity vectors to make the vortices more apparent. The upper line at each time instant is the rotating inner cylinder and the lower line is the stationary outer cylinder. The waviness of the vortices is evident in examining the motion of a single vortex. For instance, the leftmost clockwise vortex clearly moves to the right with the axial flow over one azimuthal wave period from the first frame to the last frame. But the vortex is further to the right in frame 1 than it is in frame 3 due to the azimuthal traveling waves (shown schematically in Fig. 2), which results in an axial oscillation of the vortices at a single meridional plane as the wave passes. At certain time instants, there is significant transport of fluid between vortices. The waviness of the vortices and the transport of fluid between vortices are characteristic of wavy vortex flow with no axial or radial flow [32].

The key issue with regard to rotating filtration is if the particles follow the fluid flow. Recall that three

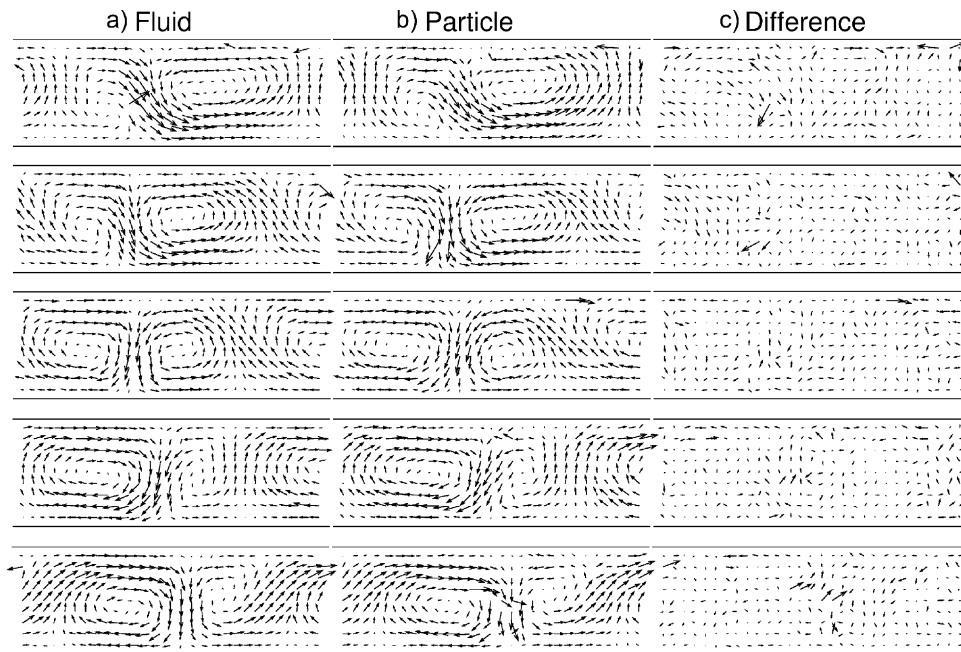


Fig. 3. The velocity field at $Re_r = 0$, $Ta = 314$, $Re_a = 3$. The axially averaged mean axial velocity is removed. Five time instants 1.0 s apart are shown with time progressing from top to bottom. Eight time instants correspond to the period of one azimuthal wave. The axial flow is left to right. The upper line in each frame is the rotating inner cylinder, and the lower line is the stationary outer cylinder: (a) fluid phase velocity; (b) particle phase velocity; and (c) slip velocity between the fluid and particle phases.

phenomena could keep particles away from the rotating filter [25]. First, Taylor vortices could wash particles off of the filter [12]. Second, back-transport of particles away from the filter surface related to the shear due to rotation of the inner cylinder and the axial cross-flow could induce migration of particles away from the filter [35]. Third, particles could sediment away from the rotating filter due to the centrifugal field. However, for the situation studied here, the density difference negligible. Thus, only the shear exclusion effect as modified by the redistribution of the azimuthal momentum by the vortices should play a role in these experiments. Fig. 3(b) shows the particle velocity field under the same conditions that fluid velocity is shown in Fig. 3(a). The particular time sequence shown in Fig. 3(b) was chosen to synchronize its phase with that shown in Fig. 3(a), but because the two velocity fields were not obtained simultaneously, the vortex size and positions match only approximately. Nevertheless, it is clear that the particles generally follow the motion of the fluid and their velocity is of similar magnitude.

It is possible, though quite difficult, to subtract the particle velocity field from the fluid velocity field to

determine the velocity difference (or “slip” velocity) between the particles and the fluid. The difficulty arises from the fluid and particle velocity fields not being obtained simultaneously due to experimental limitations. Thus, to determine the slip velocity, it is necessary to match the phase of the waviness in the fluid velocity data set to the phase in the particle velocity data set. Not only must the waviness be matched between the two data sets, but the vortices must also be aligned in the axial direction, because the vortices are traveling axially in the annulus. The tedious process of matching phase is based on visual matching and the minimization of the least squares difference between the data sets. Once the “best” match is determined, the particle velocity can be subtracted from the fluid velocity resulting in the velocity difference field shown in Fig. 3(c). Although a few large vectors appear in the slip velocity field (due to errors in the velocity measurements), most of the vectors are quite short indicating that the particles closely follow the fluid velocity.

The difference in velocity between the particles and the fluid is more easily extracted from the latitudinal plane measurements. In Fig. 4(a), the normalized

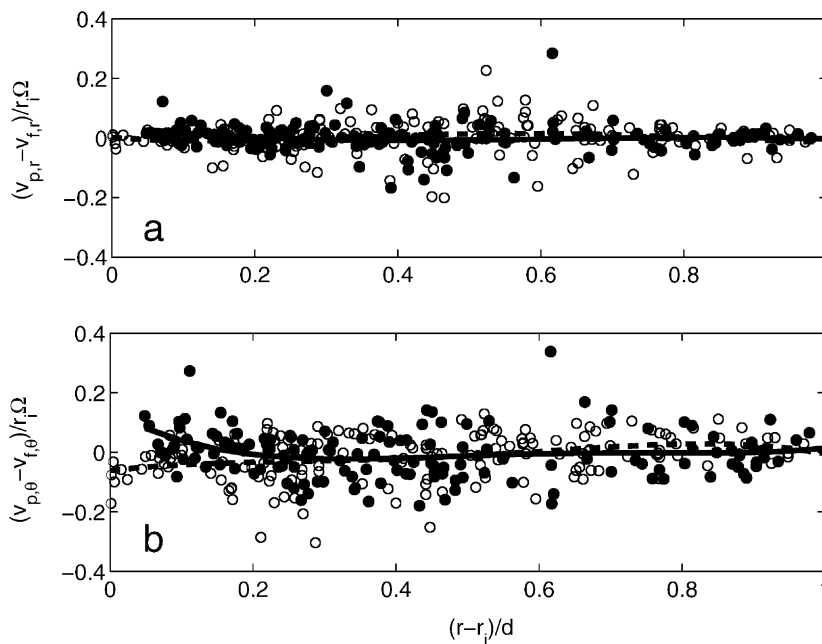


Fig. 4. Difference between the fluid and particles velocities at $Re_r = 0$, $Ta = 243$, $Re_a = 30$. (a) Radial velocity difference; (b) azimuthal velocity difference. Inflow regions: (●), (—); outflow regions: (○), (---).

radial velocity difference, $v_{p,r} - v_{f,r}$, where the p and f subscripts refer to particle and fluid velocities, is plotted as a function of normalized radial position, $(r - r_i)/d$, for $Ta = 243$. The data is plotted for two different axial positions with respect to the vortical structure of the flow: at an outflow region where fluid is flowing radially outward between vortices (open circles, dashed curve) and at an inflow region where the fluid is flowing radially inward between vortices (filled circles, solid curve). The typical velocity difference is negligible across the annular gap for both inflow and outflow regions, as indicated by the least squares curve fits. The scatter in the data shows that the fluid velocity and the particle velocity do not exactly match due to a combination of experimental error and actual velocity differences. Similar results occur for Taylor numbers of 343 and 592. The azimuthal velocity difference, $v_{p,\theta} - v_{f,\theta}$, is shown in Fig. 4(b) for $Ta = 243$. First note that the scatter in the azimuthal velocity difference is greater than that of the radial velocity difference, probably due to the higher azimuthal velocities present in the system. Like the radial velocity, the azimuthal velocity of the particles typically matches

the fluid velocity in both inflow and outflow regions, except near the inner cylinder. Within $d/4$ of the inner cylinder, the particle velocity tends to be greater than the fluid velocity in inflow regions and less than the fluid flow in outflow regions, although this result is not conclusive given the scatter in the data. This result also occurs at higher Taylor numbers of 343 and 592 with the difference as large as $0.3r_i\Omega$ at the highest Taylor number. The reason for the velocity difference is not readily apparent based on the vortical structure of the flow field. However, it is important to note that the largest velocity differences occur near the inner cylinder where the azimuthal velocity is greatest.

At this point, it is important to check if the large inertial particles should follow the flow based on a standard analysis. A simple analysis can be based on the Stokes number, $St = \rho_p D_p^2 r_i \Omega / 18 \mu d$, where ρ_p and D_p are the density and diameter of the particles, and μ is the dynamic viscosity. A large Stokes number suggests that particles cannot follow the fluid flow, while a small Stokes number suggests that the particles will follow the fluid flow. In these experiments, the Stokes number for the larger inertial particles ranged

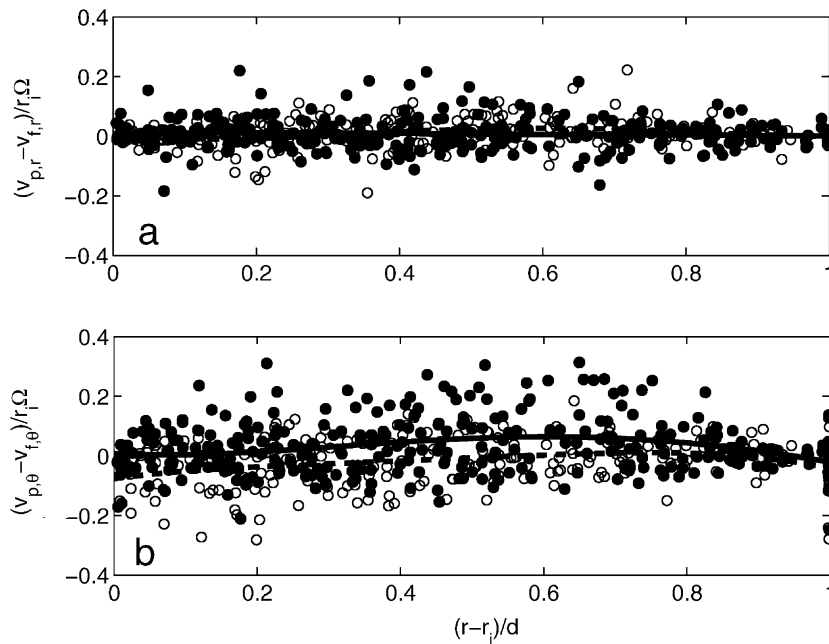


Fig. 5. Difference between the fluid and particles velocities at $Re_r = 0.2$, $Ta = 243$, $Re_a = 28$. (a) Radial velocity difference; (b) azimuthal velocity difference. Inflow regions: (●), (—); outflow regions: (○), (---).

from 0.003 to 0.083, depending upon the operating conditions. Given these Stokes numbers, the results presented above appear reasonable. That is, the particles follow the fluid flow fairly closely except near the inner cylinder where the particles are physically prevented from following the fluid through the pores of the porous cylinder.

Fig. 5 shows the fluid and particle velocity difference for a small radial flow ($Re_r = 0.2$), a moderate axial Reynolds number ($Re_a = 28$ at the axial measurement location), and a Taylor number corresponding to wavy vortices ($Ta = 243$). The radial velocities of the particles and the fluid are nearly identical across the entire gap, as shown in Fig. 5(a). The azimuthal velocity difference is also near zero across the gap as shown in Fig. 5(b), although the inflow region has a slightly larger particle velocity in the middle of the gap and the outflow region has a slightly higher fluid velocity near the inner cylinder. The scatter in the velocity difference at the outer wall may be attributed to particles rolling or sliding on the wall and to the general difficulty in extracting particle images from the PIV data near the walls. However, the scatter in the data suggests that the most reasonable conclusion that one could make is that the particle and fluid velocities are quite similar on average.

Measurements of the fluid and particle velocity fields at other combinations of Reynolds numbers and Taylor numbers are consistent with those shown in Figs. 3–5. In all cases, the particle velocity field is quite similar to the fluid velocity field. At some times the radial inflow is evident near the inner porous cylinder for $Re_r \neq 0$, especially at inflow regions between vortices. But on average the velocity difference is negligible.

4. Particle concentration profiles

The same images of the particle phase that were used to generate the particle velocity fields can also be interrogated to calculate the particle concentration profiles. To do this, the particle images were binarized by setting the pixel values below a threshold to zero and above the threshold to one. The area of contiguous pixels of high intensity was calculated. If the area was in the correct size range to be a valid particle, the centroid of the particle was recorded and used to

calculate the concentration profile. Because the radial inflow results in a decreasing volume of suspending fluid as the fluid travels axially, the increase in particle concentration with axial position depends on the axial and radial Reynolds numbers. To permit comparison of concentration profiles under different flow conditions, each profile was normalized by average concentration of particles at that particular flow condition.

The relative particle concentration profiles across the annulus for three different radial Reynolds numbers are shown in Fig. 6 for various Taylor and axial Reynolds numbers. In these figures, the radial position is normalized by the gap width [so that $(r - r_i)/d = 0$ is at the inner cylinder and $(r - r_i)/d = 1$ is at the outer cylinder], and a uniform particle distribution would correspond to a normalized concentration of unity. The situation for no radial flow is shown in Fig. 6(a) where the two lower Taylor numbers correspond to non-wavy vortical flow and the higher Taylor numbers correspond to wavy vortices. A relatively uniform particle concentration profile occurs across most of the gap regardless of flow conditions, although there appears to be a slight tendency for the concentration to decrease with radial position. This puzzling result cannot be attributed to centrifugal forces, since this would cause the particle concentration to increase with radius. The particle concentration drops substantially near either wall of the annulus. Very near the walls, the presence of the walls prevents particles from getting closer than one particle radius (about $0.015d$) from the wall. This also prevents us from measuring a particle concentration right at the walls [so the curves do not extend to $(r - r_i)/d = 0$ or 1]. However, the low particle concentration near the walls clearly extends substantially further from the wall than one particle radius. This is mostly likely a result of the Taylor vortices redistributing the azimuthal momentum such that it is nearly uniform across the gap with steep gradients of azimuthal velocity in the radial direction near both the inner and outer cylinders [22,24,32]. This azimuthal velocity gradient along with the axial velocity gradient from the imposed axial flow causes large shear rates near both cylinders out of which particles tend to migrate. Based on the results shown in Fig. 6(a), the region of reduced particle concentration is about $0.1d$ thick. This thickness is about half the thickness of the region having the steepest azimuthal velocity gradient at this Taylor number.

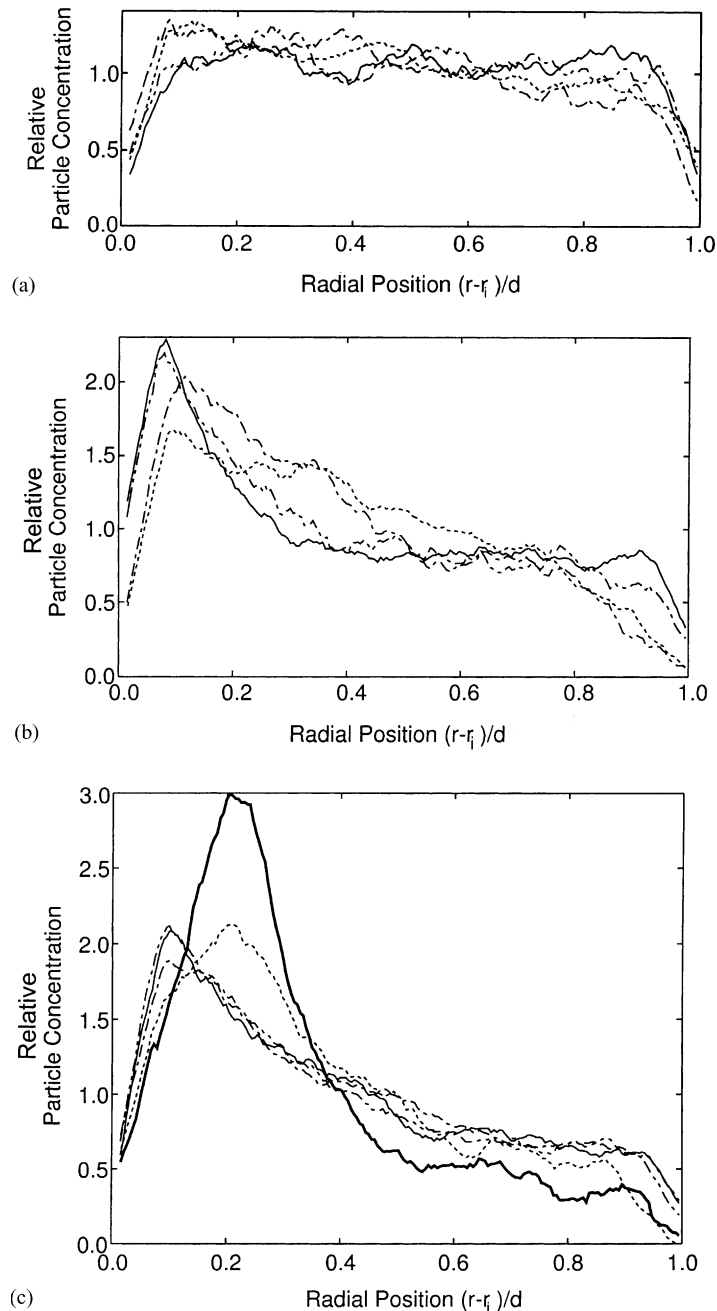


Fig. 6. Relative particle concentration profiles across the annular gap: (a) no radial flow, $Re_r = 0$: (----) $Ta = 102$ (non-wavy vortices), $Re_a = 3$; (—) $Ta = 134$, $Re_a = 17$ (non-wavy vortices); (---) $Ta = 314$, $Re_a = 16$ (wavy vortices); (-----) $Ta = 314$, $Re_a = 3$ (wavy vortices); (b) small radial flow, $Re_r = 0.1$: (----) $Ta = 110$, $Re_a = 3$ (non-wavy vortices); (---) $Ta = 132$, $Re_a = 19$ (non-wavy vortices); (—) $Ta = 877$, $Re_a = 9$ (wavy vortices); (-----) $Ta = 877$, $Re_a = 22$ (wavy vortices); (c) large radial flow, $Re_r = 0.8$: (—) $Ta = 165$, $Re_a = 57$ (no vortices); (----) $Ta = 248$, $Re_a = 33$ (wavy vortices); (---) $Ta = 248$, $Re_a = 57$ (wavy vortices); (—) $Ta = 1650$, $Re_a = 42$ (weakly turbulent vortices); (-----) $Ta = 1650$, $Re_a = 67$ (weakly turbulent vortices).

Although the thickness of the layer of reduced particle concentration is less than the thickness of the steep velocity gradient region, it is likely that the two are related.

When the radial flow is non-zero, the particle concentration profiles change substantially as shown in Fig. 6(b). The two lower Taylor numbers in the figure correspond to non-wavy vortices just above the transition to vortical flow, while the two higher Taylor numbers correspond to wavy vortices. Again the particle concentration is lower near the walls for the same reasons as in Fig. 6(a), indicating that the steep velocity gradients due to the vortical transport of the azimuthal momentum is still effective in keeping particles away from the porous inner cylinder, even with radial flow. But in this case, there is a high particle concentration just outside of the particle exclusion region near the inner cylinder that decreases radially outward to about one-half of the distance across the gap. From this point outward the particle concentration is nearly constant until near the outer cylinder. Clearly, the radial inflow works against the vortical transport to carry particles toward the inner cylinder.

Substantially higher radial flows, shown in Fig. 6(c), also exhibit elevated concentrations in the near the inner cylinder and lower concentrations near the outer cylinder. Note that the axial Reynolds numbers are necessarily higher in this case than in the $Re_r = 0.1$ case to provide adequate axial flow to supply the large radial flow through the porous inner cylinder. For the lowest Taylor number (solid curve), the particle concentration, while low adjacent to the inner cylinder, is much higher in the region near the inner cylinder and lower near the outer cylinder than the other cases. This result can be explained by the absence of vortices that act to redistribute the particles radially at this Taylor number. Since there are no vortices, particles accumulate near the inner cylinder. At higher Taylor numbers, the vortical flow redistributes particles across the annular gap. Thus, while the particles are excluded from the immediate vicinity of the porous inner cylinder as a result of the steep azimuthal velocity gradient regardless of whether vortices are present or not, the vortices redistribute the particles toward the outer portions of the annulus reducing the build-up of high particle concentrations near the inner cylinder.

5. Cake formation and particle resuspension

As filtration progresses, a cake layer builds up on the surface of the inner porous cylinder. A comparison between situations with no radial flow and with radial flow ($Re_r = 0.1$) are shown in Fig. 7 for $Ta = 214$ in the latitudinal plane experiments. In these photos, the thin curve at the top of the image is the outer cylinder and that at the bottom of the image is the porous inner cylinder. The build-up of the cake layer is quite evident for the case of radial flow in spite of the lower particle concentration adjacent to the filter surface evident in Fig. 6, because particles are carried onto the filter surface by the radial flow through the filter. The largest volume of particles on the surface of the porous cylinder consisted of the larger inertial particles, but many smaller PIV tracer particles were also in the cake.

The growth of the cake layer thickness was measured by counting the bright pixels corresponding to particles at the porous inner cylinder using similar images to those shown in Fig. 7. The results are shown in Fig. 8 for three Taylor numbers and an initial radial Reynolds number of $Re_r = 0.25$. The polynomial curve fits through the data are only to guide the eye, not to suggest a form for the transient behavior of the cake layer thickness. Since a constant pressure was used in these experiments, the radial Reynolds number decreases to 38% of its initial value as particles build up on the filter surface and the flux declined. The cake layer thickness initially increases and then levels off. As the rotational speed increases, the cake layer thickness is reduced, probably as a consequence of the combined effects of rotational shear and the redistribution of azimuthal momentum, both acting to increase the shear at the inner cylinder [25]. At the lowest rotational speed ($Ta = 214$), the cake layer is about 3–4 particles thick. As the rotational speed increases, the cake layer is reduced to <2 particle diameters thick for $Ta = 428$ and close to one particle thick for $Ta = 642$.

In the meridional plane experiments, we noticed that increasing the speed of the inner cylinder after the deposition of the cake layer resulted in the removal of particles, as shown in Fig. 9. In all three images, the bright line at the top of the image is the rotating inner cylinder and the dark line at the bottom of the image is the stationary outer cylinder. The particles

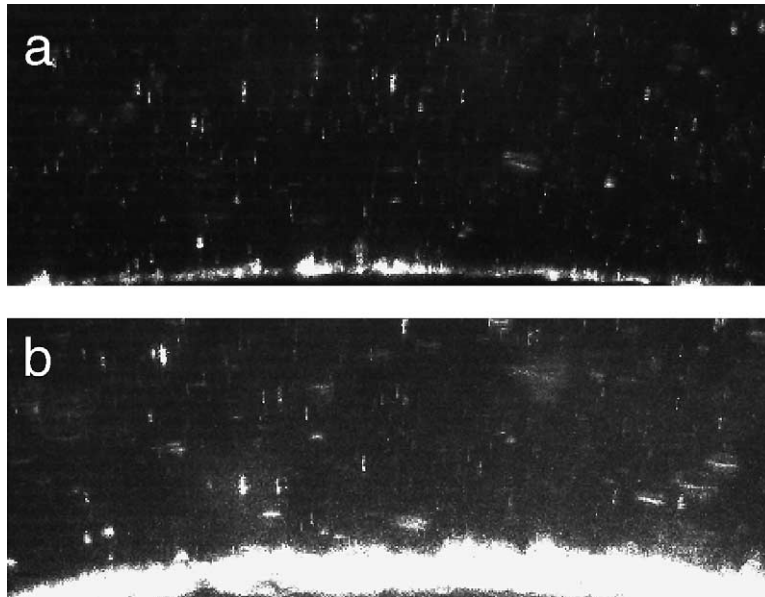


Fig. 7. The build-up of a cake layer on the inner cylinder at $Ta = 214$ and $Re_a = 29$: (a) $Re_r = 0$; (b) $Re_r = 0.1$. The curved surfaces of the outer (top of the image) and inner (bottom of the image) are evident.

were allowed to collect on the inner cylinder due to a radial flow corresponding to $Re_r = 0.86$ at a Taylor number for which the flow was non-vortical. Then the rotational speed of the inner cylinder was increased. In Fig. 9(a) where $Ta = 490$ (corresponding to wavy vortical flow), most particles remain caked on the inner cylinder. But at $Ta = 750$, many particles are caught in

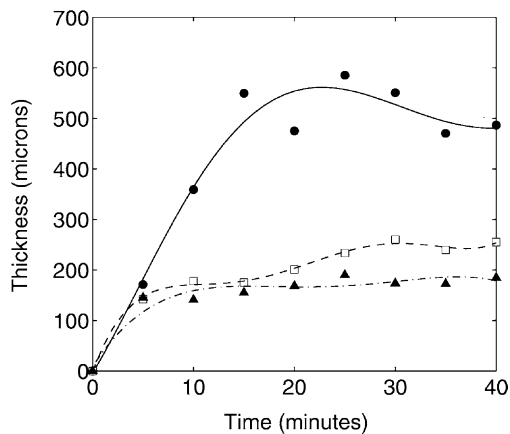


Fig. 8. Cake layer thickness as a function of time for $Re_a = 30$ and $Re_r = 0.25$ initially: (●) $Ta = 214$; (□) $Ta = 423$; (▲) $Ta = 642$.

the vortical flow as shown in Fig. 9(b). Most particles seem to be at the periphery of the vortices with few particles near the vortex centers consistent with other recent experimental results [36] and simulations [26]. Increasing the Taylor number to 875 removes more particles from the inner cylinder, as shown in Fig. 9(c), and distributes them throughout the vortices, probably as a result of chaotic mixing inherent in wavy Taylor vortex flow [37–39].

To quantify these observations, a layer of particles was allowed to form on the inner cylinder at a low rotational speed and then the speed was ramped up to determine the Taylor number where particles were swept off of the inner cylinder. Three radial Reynolds numbers, $Re_r = 0.1, 0.48, 0.86$, were used to span the range frequently used in commercial separators [6,9,14,20,21,40]. A variety of axial Reynolds numbers were considered. The experiment began by setting the radial and axial Reynolds numbers at the desired values with the inner cylinder turning at a slow enough rate so that the flow was non-vortical ($Ta = 44$) for about 10 min to permit a layer of particles to accumulate. Then the inner cylinder rotation rate was ramped so that the Taylor number increased at a rate of 14 Ta per second while images of the particles in the

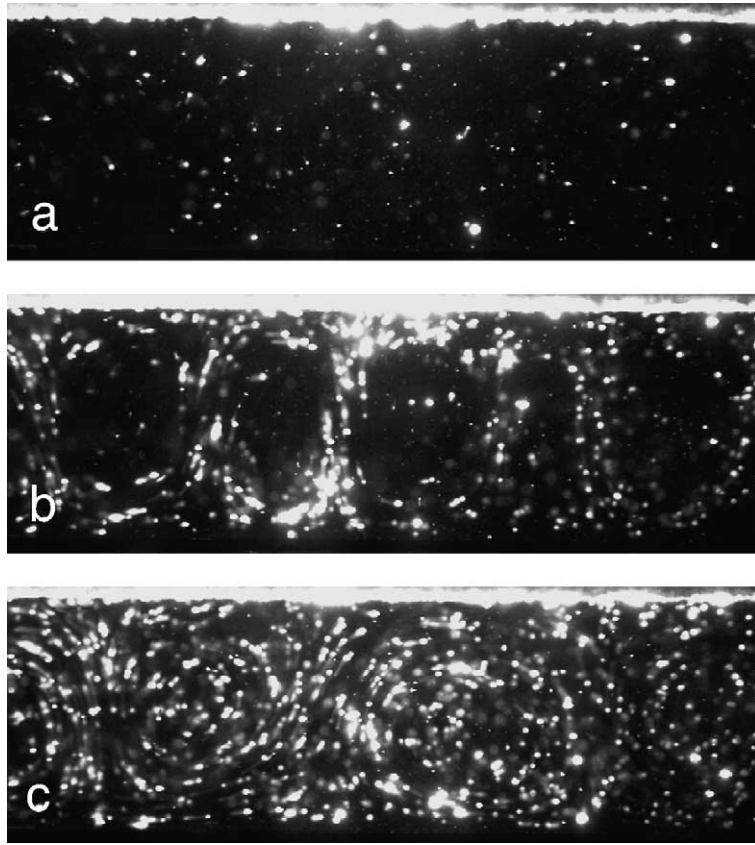


Fig. 9. Images of the particles in the annulus for $Re_r = 0.86$, $Re_a = 11$: (a) $Ta = 490$, (b) $Ta = 750$, (c) $Ta = 875$.

annulus (like those in Fig. 9) were recorded at 0.75 Hz. A small number of tests at twice the acceleration produced similar results, indicating that the acceleration was not a key parameter. The images of particles in the annulus were analyzed to determine the particle concentration in the annulus as a function of the linearly increasing Taylor number. A typical result is shown in Fig. 10 where the jagged curves are the data and the solid lines are fits to the data. At low Taylor numbers, the particle concentration in the annulus remains constant indicating that particles initially trapped in the cake layer on the inner cylinder remain trapped. However, once the Taylor number is exceeded particular value (in this case, just >500), the particle concentration in the annulus increases linearly with Taylor number indicating the particles initially trapped on the inner cylinder were increasingly resuspended.

Repeating this resuspension experiment for several axial and radial Reynolds numbers permitted the evaluation of the effect of these parameters on the Taylor number at which the particles begin to resuspend (the knee in the curve in Fig. 10 as defined by the intersection of the horizontal line and the angled line), as shown in Fig. 11. The line corresponds to a linear regression fit to the data. The wide scatter in the data is a consequence of the wide range of parameters ($3 \leq Re_a \leq 62$; $0.1 \leq Re_r \leq 0.86$). Nevertheless, it is immediately evident that higher radial Reynolds numbers require a greater Taylor number to resuspend particles because of the higher suction at the porous inner cylinder. In addition, higher axial Reynolds numbers also require higher Taylor numbers to resuspend the particles. At first glance, this result is surprising since one would expect that the higher

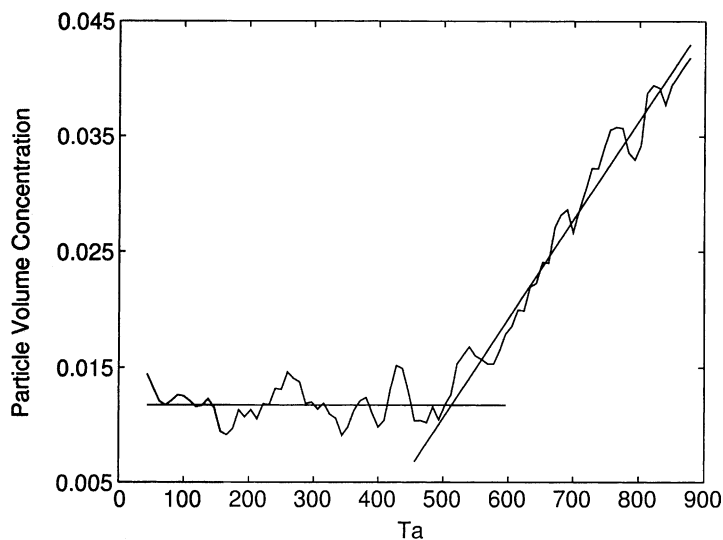


Fig. 10. Sample of the particle volume concentration in the annulus as the Taylor number is increased at $Re_a = 11$ and $Re_r = 0.86$.

axial shear would more easily dislodge the particles from the inner cylinder. But experiments measuring the velocity field in Taylor vortex flow with axial and radial flow indicate that the time-averaged azimuthal velocity gradients at the inner cylinder decrease with increasing Taylor number because of vortical transport [41]. Thus, a higher shear stress occurs at a lower

axial Reynolds number dislodging particles from the inner cylinder at a lower Taylor number.

We recently proposed a dimensionless parameter related to the degree to which particles reach the surface of a rotating filter [25]. The force that induces the mass transport of particles toward the filter surface is the Stokes drag due to the filtrate flux. The Stokes drag perpendicular to the filter surface is counteracted by shear stress, which acts parallel to the filter surface, resulting in migration of particles away from the filter surface. The ratio between the shear force and the Stokes drag for the geometry of a rotating filter can be written as

$$\frac{F_\tau}{F_D} = \frac{\Omega r_i D_p}{3Ud} = \frac{Ta D_p}{3Re_r d}$$

We found that when this number was of order 20 or greater, the build-up of a cake layer on the surface of the rotating filter was minimal. For the data plotted in Fig. 11, this ratio was from 6 to 11 for all cases except those at the lowest radial Reynolds number, where the ratio was 43 and 46. The results in Fig. 11 falling within less than an order of magnitude of 20 offers further support that the ratio of the shear force to the Stokes drag is the key dimensionless parameter related to the deposition of particles on the surface of a rotating filter.

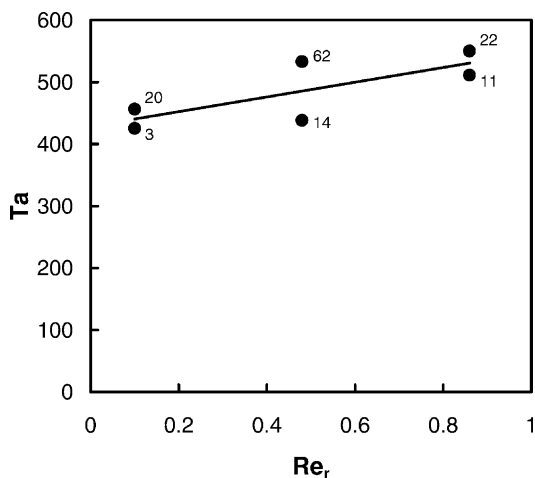


Fig. 11. Taylor number at which initially deposited on the inner cylinder are washed off with a linear regression fit to the data. Re_a is noted next to the data points.

6. Conclusions

The measurements described here provide direct evidence of the physical mechanisms at work in a rotating filter. The velocity fields of the particles and the fluid are quite similar resulting in negligible slip velocity. Thus, the particles largely follow the fluid flow. The particle concentration profiles at zero radial flow indicate that the particles are excluded from near the wall, probably due to a combination of the large velocity gradient near the wall and the vortical flow. For vortical flows in the presence of a radial inflow, there is a peak in the concentration profiles near the inner cylinder, but this peak is much smaller than when no vortices are present indicating that vortices aid in transporting particles away from the inner cylinder. Once the particles are deposited on the inner cylinder due to the radial flow, increasing the Taylor number above a critical value results in sweeping the particles off the inner cylinder to resuspend them in the vortical flow. This critical Taylor number not only increases with increasing radial Reynolds number as expected, but also increases with increasing axial Reynolds number due to the reduced azimuthal velocity gradient at higher axial Reynolds numbers. An important limitation in the applicability of the results of this research is that the inertial particles considered here were fairly large (150–300 μm). Thus, while the general results are likely applicable to microfiltration where the particles are typically $<10 \mu\text{m}$ in diameter, the details of the back-transport mechanisms at the filter surface may be substantially different.

These results suggest the following model for the motion of particles in a rotating filter. The radial flow carries particles toward the inner porous cylinder. This radial flow is opposed by the centrifugal force acting radially outward on the particle, which is quite small in this case because of the small difference in the particle and fluid densities. The rotation of the inner cylinder results in a velocity gradient near the inner cylinder that leads to a reduced particle concentration near the inner cylinder. The azimuthal velocity gradient is enhanced near the inner cylinder due to the vortical motion transporting fluid with high azimuthal momentum outward from the inner cylinder and low azimuthal momentum fluid inward from the outer cylinder. This results in a nearly uniform azimuthal velocity near across the annulus with very steep azimuthal velocity

gradients near the cylinders. This steep velocity gradient is very effective in keeping particles away from the inner cylinder and removing particles from the inner cylinder that were carried there by the radial flow. Then the vortical motion in the annulus carries the particles across the annulus further reducing the particle concentration near the inner cylinder. As a result of these mechanisms, the particles are less likely to foul the filter than in standard cross-flow filtration.

Acknowledgements

Support by the National Science Foundation is gratefully acknowledged. We thank Professor Edwin A. Cowen of Cornell University for providing the particle tracking velocimetry code and the reviewers for their helpful suggestions.

References

- [1] B. Hallström, M. Lopez-Leiva, Description of a rotating ultrafiltration module, *Desalination* 24 (1978) 273–279.
- [2] A. Margaritis, C.R. Wilke, The Rotorfermentor. I. Description of the apparatus, power requirements, and mass transfer characteristics, *Biotech. Bioeng.* 20 (1978) 709–726.
- [3] F. Vigo, C. Uliana, P. Lupino, The performance of a rotating module in oily emulsions ultrafiltration, *Separat. Sci. Tech.* 20 (1985) 213–230.
- [4] K.H. Kroner, V. Nissinen, H. Ziegler, Improved dynamic filtration of microbial suspensions, *BioTechnology* 5 (1987) 921–926.
- [5] K.H. Kroner, V. Nissinen, Dynamic filtration of microbial suspensions using an axially rotating filter, *J. Membr. Sci.* 36 (1988) 85–100.
- [6] K. Ohashi, K. Tashiro, F. Kushiya, T. Matsumoto, S. Yoshida, M. Endo, T. Horio, K. Ozawa, K. Sakai, Rotation-induced Taylor vortex enhances filtrate flux in plasma separation, *Trans. Am. Soc. Artif. Intern. Organs* 34 (1988) 300–307.
- [7] S. Wronski, E. Molga, L. Rudniak, Dynamic filtration in biotechnology, *Bioprocess Eng.* 4 (1989) 99–104.
- [8] D.W. Schoendorfer, Method and apparatus for separation of matter from suspension, US Patent (1993) 5,194,145.
- [9] G. Beaudoin, M.Y. Jaffrin, Plasma filtration in Couette flow membrane devices, *Artif. Organs* 13 (1989) 43–51.
- [10] M. Lopez-Leiva, Ultrafiltration at low degrees of concentration polarization: technical possibilities, *Desalination* 35 (1980) 115–128.
- [11] F. Vigo, C. Uliana, Influence of the vorticity at the membrane surface on the performances of the ultrafiltration rotating module, *Separat. Sci. Tech.* 21 (1986) 367–381.

- [12] J.R. Hildebrandt, J.B. Saxton, The use of Taylor vortices in protein processing to enhance membrane filtration performance, in: J.R.C. Dean, R.M. Nerem (Eds.), *Bioprocess Engineering Colloquium*, The American Society of Mechanical Engineers, New York, 1987, pp. 93–95.
- [13] W. Goldinger, E. Rebsamen, E. Brandli, H. Ziegler, *Dynamische mikro-und ultrafiltration in der biotechnologie*, *Technische Rundschau Sulzer* 3 (1986) 10–12.
- [14] U.B. Holeschovsky, C.L. Cooney, Quantitative description of ultrafiltration in a rotating filtration device, *AIChE J.* 37 (1991) 1219–1226.
- [15] R.O. Gilcher, Plasmapheresis technology, *Vox Sang* 51 (Suppl. 1) (1986) 35–39.
- [16] P. Perseghin, A. Pagani, P.M. Fornasari, L. Salvaneschi, Donor plasmapheresis: a comparative study using four different types of equipment, *Int. J. Artif. Organs* 10 (1987) 51–56.
- [17] G. Vezon, Y. Piquet, C. Manier, F. Schooneman, F. Mesnier, J. Moulinier, Technical aspects of different donor plasmapheresis systems and biological results obtained in collected plasma, *Vox Sang* 51 (Suppl. 1) (1986) 40–44.
- [18] M. Jaffrin, G. Beaudoin, L.H. Ding, N. Djennaoui, Effect of membrane characteristics on the performance of Couette rotating plasma separation devices, *Trans. Am. Soc. Artif. Intern. Organs* 35 (1989) 690–693.
- [19] R.J. Fischel, H. Fischel, A. Schatzel, W.P. Lange, D. Cahill, D. Gervais, N.L. Ascher, Couette membrane filtration with constant shear stress, *Trans. Am. Soc. Artif. Intern. Organs* 34 (1988) 375–385.
- [20] G. Belfort, J.M. Pimbley, A. Greiner, K.Y. Chung, Diagnosis of membrane fouling using a rotating annular filter. 1. Cell culture media, *J. Membr. Sci.* 77 (1993) 1–22.
- [21] G. Belfort, P. Mikulasek, J.M. Pimbley, K.Y. Chung, Diagnosis of membrane fouling using a rotating annular filter. 2. Dilute particle suspensions of known particle size, *J. Membr. Sci.* 77 (1993) 23–39.
- [22] P.S. Marcus, Simulation of Taylor–Couette flow. Part 2. Numerical results for wavy-vortex flow with one travelling wave, *J. Fluid Mech.* 146 (1984) 65–113.
- [23] S.T. Wereley, R.M. Lueptow, Azimuthal velocity in supercritical circular Couette flow, *Exp. Fluids* 18 (1994) 1–9.
- [24] A. Akonur, R.M. Lueptow, Three-dimensional velocity field for non-wavy and wavy Taylor–Couette flow, *Phys. Fluids*, submitted for publication.
- [25] J.A. Schwille, D. Mitra, R.M. Lueptow, Design parameters for rotating filtration, *J. Membr. Sci.* 204 (2002) 53–65.
- [26] S.T. Wereley, R.M. Lueptow, Inertial particle motion in a Taylor–Couette rotating filter, *Phys. Fluids* 11 (1999) 325–333.
- [27] J. Parker, P. Merati, An investigation of turbulent Taylor–Couette flow using laser Doppler velocimetry in a refractive index matched facility, *J. Fluids Eng.* 118 (1996) 810–818.
- [28] R.P. Dring, Sizing criteria for laser anemometry particles, *ASME J. Fluid Eng.* 104 (1982) 15–17.
- [29] E.A. Cowen, S.G. Monismith, A hybrid digital particle tracking velocimetry technique, *Exp. Fluids* 22 (1997) 199–211.
- [30] E.C. Johnson, R.M. Lueptow, Hydrodynamic stability of flow between rotating porous cylinders with radial and axial flow, *Phys. Fluids* 9 (1997) 3687–3696.
- [31] G.P. King, Y. Li, W. Lee, H.L. Swinney, P.S. Marcus, Wave speeds in wavy Taylor-vortex flow, *J. Fluid Mech.* 141 (1984) 365–390.
- [32] S.T. Wereley, R.M. Lueptow, Spatio-temporal character of supercritical circular Couette flow, *J. Fluid Mech.* 364 (1998) 59–80.
- [33] R.M. Lueptow, A. Docter, K. Min, Stability of axial flow in an annulus with a rotating inner cylinder, *Phys. Fluids A* 4 (1992) 2446–2455.
- [34] S.T. Wereley, R.M. Lueptow, Velocity field for Taylor–Couette flow with an axial flow, *Phys. Fluids* 11 (1999) 3637–3649.
- [35] G. Belfort, R.H. Davis, A.L. Zydney, The behavior of suspensions and macromolecular solutions in cross-flow microfiltration, *J. Membr. Sci.* 96 (1994) 1–58.
- [36] X.T. Chen, T.S. Yang, S.S. Shy, Preferential concentration of heavy particles in a Taylor–Couette flow, *Bull. Am. Phys. Soc.* 46 (10) (2001) 72.
- [37] M. Rudman, Mixing and particle dispersion in the wavy vortex regime of Taylor–Couette flow, *AIChE J.* 44 (1998) 1015–1026.
- [38] M. Rudolph, T. Shinbrot, R.M. Lueptow, A model of mixing and transport in wavy Taylor–Couette flow, *Physica D* 121 (1998) 163–174.
- [39] A. Akonur, R.M. Lueptow, Chaotic mixing and transport in wavy Taylor–Couette flow, *Physica D* (2002), in press.
- [40] W. Tobler, Dynamic filtration: principle and application of shear filtration in an annular gap, *Filtrat. Separat.* 19 (1982) 329–332.
- [41] K. Min, R.M. Lueptow, Circular Couette flow with pressure-driven axial flow and a porous inner cylinder, *Exp. Fluids* 17 (1994) 190–197.